Interplay of lattice, electronic, and spin degrees of freedom in detwinned $BaFe_2As_2$: A Raman scattering study

A. Baum,[1,2] Ying Li,[3] M. Tomić,[3] N. Lazarević,[4] D. Jost,[1,2] F. Löffler,[1,2] B. Muschler,[1,2,*] T. Böhm,[1,2,†] J.-H. Chu,[5,6,7] I. R. Fisher,[5,6] R. Valentí,[3] I. I. Mazin,[8] and R. Hackl[1,‡]

[1]*Walther Meissner Institut, Bayerische Akademie der Wissenschaften, 85748 Garching, Germany*
[2]*Fakultät für Physik E23, Technische Universität München, 85748 Garching, Germany*
[3]*Institut für Theoretische Physik, Goethe-Universität Frankfurt, Max-von-Laue-Straße 1, 60438 Frankfurt am Main, Germany*
[4]*Center for Solid State Physics and New Materials, Institute of Physics Belgrade, University of Belgrade, Pregrevica 118, 11080 Belgrade, Serbia*
[5]*Stanford Institute for Materials and Energy Sciences, SLAC National Accelerator Laboratory, 2575 Sand Hill Road, Menlo Park, California 94025, USA*
[6]*Geballe Laboratory for Advanced Materials & Dept. of Applied Physics, Stanford University, California 94305, USA*
[7]*Department of Physics, University of Washington, Seattle, Washington 98195, USA*
[8]*Code 6393, Naval Research Laboratory, Washington, DC 20375, USA*

(Received 13 June 2018; revised manuscript received 18 July 2018; published 7 August 2018)

We report results of Raman scattering experiments on twin-free $BaFe_2As_2$ with the main focus placed on understanding the influence of electronic and spin degrees of freedom on the lattice dynamics. In particular, we scrutinize the E_g modes and the As A_{1g} mode. Each of the two E_g phonons in the tetragonal phase is observed to split into a B_{2g} and a B_{3g} mode upon entering the orthorhombic stripe-magnetic phase. The splitting amounts to approximately 10 cm^{-1} and less than 5 cm^{-1} for the low- and the high-energy E_g mode, respectively. The detailed study of the fully symmetric As mode using parallel incident and outgoing photon polarizations along either the antiferromagnetic or the ferromagnetic Fe-Fe direction reveals an anisotropic variation of the spectral weight with the energy of the exciting laser indicating a polarization-dependent resonance effect. Along with the experiments we present results from density functional theory calculations of the phonon eigenvectors, the dielectric function, and the Raman tensor elements. The comparison of theory and experiment indicates that (i) orbital-selective electronic correlations are crucial to understand the lattice dynamics and (ii) all phonon anomalies originate predominantly from the magnetic ordering and the corresponding reconstruction of the electronic bands at all energies.

DOI: 10.1103/PhysRevB.98.075113

I. INTRODUCTION

One of the most debated issues in Fe-based superconductors is the interplay of spin, orbital, and lattice degrees of freedom at the onset of magnetism, nematicity, and superconductivity [1–5], particularly interplay between phonons and magnetic degrees of freedom. For instance, soon after the discovery of Fe-based superconductors, the magnetic moment was predicted to couple to the As position [6]. Zbiri *et al.* found a modulation of the electronic density of states (DOS) at the Fermi energy E_F by the two E_g and the A_{1g} modes [7]. Various anomalies were observed experimentally using neutron, Raman, and optical spectroscopy [8–15] but are not fully understood yet.

One particular effect is the observation of substantial Raman scattering intensity of the As phonon below the magnetostructural transition in crossed polarizations with the electric fields oriented along the axes of the pseudo-tetragonal 2 Fe unit cell [9] [for the definition of the axes see Fig. 1(a)]. From the weak coupling point of view, it has been argued that the formation of a spin-density wave (SDW) modifies the low-energy electronic structure near the Fermi level, and this modification leads to the anomalous intensity [16]. On the other hand, recent experiments were interpreted by introducing a phenomenological coupling between the phonon and the particle-hole continuum scaling with the amplitude of ordered magnetic moment [17] being on the order of 1 μ_B. This approach is clearly beyond the weak-coupling regime. Density functional (DFT) calculations and general considerations suggest that substantial modifications of the electronic structure occur in a broad energy range of order $J_{Hund} \gtrsim 1$ eV, corresponding to the Raman *photon* (as opposed to phonon) energy scale. This raises suspicion that a quantitative description of the modifications in the Raman spectra upon magnetic ordering should take into account the broad energy range covering the entire $d-$ electron band widths. Unfortunately, previous studies were done either in twinned samples or using only a single excitation energy, which limited the scope of experimental data being, as

*Present address: Zoller & Fröhlich GmbH, Simoniusstrasse 22, 88239 Wangen im Allgäu,Germany
†Present address: TNG Technology Consulting GmbH, Beta-Straße, 85774 Unterföhring, Germany
‡hackl@wmi.badw.de

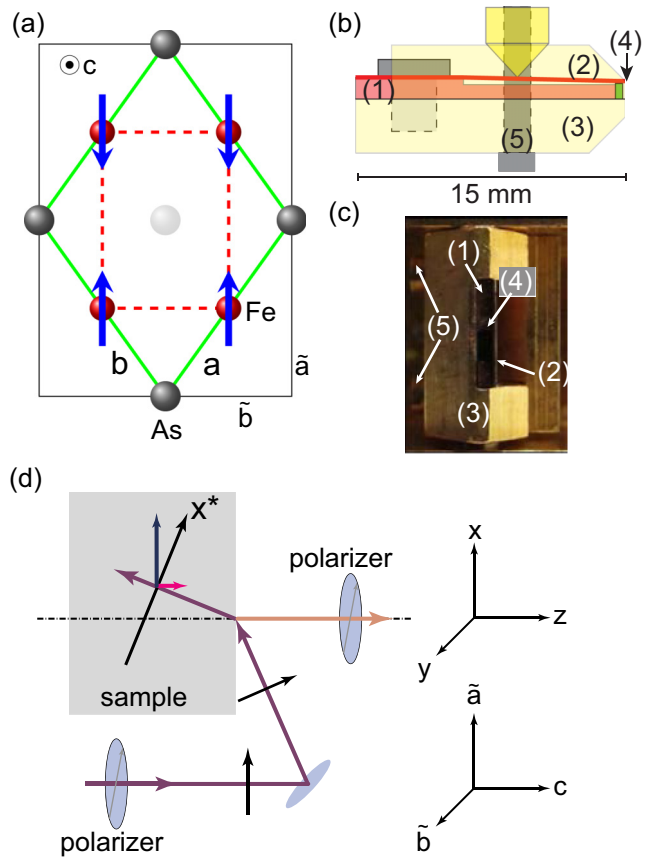

FIG. 1. FeAs layer of $BaFe_2As_2$ and detwinning clamp. (a) The As-atoms (grey) in the center and at the edges are below and, respectively, above the Fe plane (red). For this reason, the 2 Fe unit cell with the axes a and b (green) is determined by the As atoms. In the orthorhombic phase, the Fe-Fe distances become inequivalent with the distortion strongly exaggerated here. The magnetic unit cell is twice as large as the 2 Fe unit cell and has the axes $\tilde{a}$ and $\tilde{b}$. (b) Schematic sketch and (c) photograph of the detwinning clamp. The sample (4) is glued on the copper plate (1), which is in good thermal contact with the sample holder (3). Upon tightening the screws (5), the force exerted by the copper-beryllium cantilever (2) can be adjusted. (d) Schematic representation of the geometry of our Raman scattering experiment. All incoming light polarizations $\mathbf{e}_\mathrm{I}$ which are not parallel to y have finite projections on the c axis (red arrow).

a result, not sufficiently restrictive to different, maybe even contradictory, interpretations.

In this paper, we systematically address this issue experimentally, using detwinned samples and resonant Raman scattering, and interpret the results quantitatively, not on a phenomenological or model level, but using DFT calculations. Our two most vital conclusions are that (i) magnetism affects *all* Fe bands in an essential way and that has to be accounted for in explaining Raman efficiencies and (ii) the fact that Fe d states are correlated on a moderate, but considerable level, while As p states are not, is not just quantitatively, but qualitatively important in understanding the resonant behavior.

A key issue hindering straightforward DFT calculations is the fact that the *high-temperature tetragonal* phase is paramagnetically disordered, and cannot be simulated by calculations with suppressed local magnetism [18]. As explained in detail below, we circumvented this problem by assuming a magnetic order that preserves the large (albeit probably still somewhat underestimated) magnetic moment but respects the tetragonal symmetry. Yet another issue was to account for the correlation-driven renormalization of the $d-$band width. To this end, we separated the energy bands into two windows, a high-energy one dominated by As and a low-energy one derived predominantly from Fe. The Fe states were then uniformly renormalized. With these two assumptions, we could reproduce (i) the positions of the Raman-active phonons and their splitting and evolution in the detwinned orthorhombic antiferromagnetic state and (ii) Raman intensities, including the $\tilde{a}-\tilde{b}$ anisotropy as well as the complex resonant evolution with the laser light energy $\hbar\omega_\mathrm{I}$. While it is not clear *a priori* that the two computational tricks described above are sufficiently accurate, even being physically motivated, the results provide an experimental justification and convincingly substantiate the underlying physical concepts: the pivotal role of local moments in the lattice dynamics of Fe-based superconductors, and the importance of band renormalizations for d-electrons. This said, further calculations avoiding these approximations, such as full-scale dynamical mean-field theory (DMFT) computations, are quite desirable but are beyond the scope of this work.

II. METHODS

A. Samples

The $BaFe_2As_2$ crystal was prepared using a self-flux technique. Details of the crystal growth and characterization are described elsewhere [19]. $BaFe_2As_2$ is a parent compound of double-layer iron-based superconductors and orders in a stripelike SDW below $T_\mathrm{SDW} \approx 135$ K. Superconductivity can be obtained by substituting any of the ions or by pressure [20]. In $Ba(Fe_{1-x}Co_x)_2As_2$ ($0 < x \lesssim 0.06$), the SDW is preceded by a structural phase transition from a tetragonal ($I4/mmm$) to an orthorhombic ($Fmmm$) lattice at $T_\mathrm{s} > T_\mathrm{SDW}$ [19]. It remains a matter of debate as to whether or not T_SDW and T_s coincide in $BaFe_2As_2$ [19,21].

Figure 1(a) shows the relation of the various axes. The axes of the tetragonal crystal ($T > T_\mathrm{s}$, green lines) are denoted a and b with $a = b$. The axes of the magnetically ordered structure (4 Fe per unit cell, black lines), $\tilde{a}$ and $\tilde{b}$, differ by approximately 0.7% below T_SDW [22] and the Fe-Fe distance along the $\tilde{b}$ axis becomes shorter than along the $\tilde{a}$ axis as sketched in Fig. 1(a). As a result, the angle between a and b differs from 90° by approximately 0.4°.

Below T_SDW, the spins order ferromagnetically along $\tilde{b}$ and antiferromagnetically along $\tilde{a}$. Due to the small difference between $\tilde{a}$ and $\tilde{b}$, the crystals are twinned below T_s, and the orthogonal $\tilde{a}$ and $\tilde{b}$ axes change roles at twin boundaries running along the directions of the tetragonal a and b axes. The orthorhombic distortion makes the proper definition of the axes important as has been shown for twin-free crystals by longitudinal and optical transport as well as by ARPES [23–28]. To obtain a single-domain orthorhombic crystal, we constructed a sample holder for applying uniaxial pressure parallel to the Fe-Fe direction.

B. Detwinning clamp

The detwinning clamp is similar to that used by Chu *et al.* [23]. Figures 1(b) and 1(c) show, respectively, a schematic drawing and a photograph of the clamp. The sample is attached to a thermally sinked copper block (1) with GE varnish, which remains sufficiently elastic at low temperatures and maintains good thermal contact between the holder (3) and the sample (4). The stress is applied using a copper-beryllium cantilever (2), which presses the sample against the body of the clamp. Upon tightening the screws (5), the force on the sample can be adjusted. In our experiment, the pressure is applied along the Fe-Fe bonds. The c axis of the sample is perpendicular to the force and parallel to the optical axis. The uniaxial pressure can be estimated from the rate of change of the tetragonal-to-orthorhombic phase transition at T_s. Using the experimentally derived rate of 1 K per 7 MPa [29,30], we find approximately 35 MPa for our experiment to be sufficient to detwin the sample.

C. Light scattering

The experiment was performed with a standard light scattering setup. We used two ion lasers (Ar^+ Coherent Innova 304C and Kr^+ Coherent Innova 400) and two diode pumped solid state lasers (Coherent Genesis MX SLM, Laser Quantum Ignis) providing a total of 14 lines ranging from 407 nm to 676 nm, corresponding to incident energies $\hbar\omega_I$ between 3.1 and 1.8 eV. Due to this wide range, the raw data have to be corrected. The quantity of interest is the response function $R\chi''(\Omega)$ where $\Omega = \omega_I - \omega_S$ is the Raman shift, ω_S is the energy of the scattered photons and R is an experimental constant. Details of the calibration are described in Appendix A.

Application of the Raman selection rules requires well-defined polarizations for the exciting and scattered photons. The polarizations are given in Porto notation with the first and the second symbol indicating the directions of the incoming and scattered photons' electric fields $\mathbf{e}_I$ and $\mathbf{e}_S$, respectively. We use xyz for the laboratory system [see Fig. 1(d)]. The xz plane is vertical and defines the plane of incidence, yz is horizontal, xy is the sample surface, and the z axis is parallel to the optical axis and to the crystallographic c axis. For the sample orientation used here (see Fig. 1), the Fe-Fe bonds are parallel to x and y, specifically $\tilde{a} = (1, 0, 0) \parallel x$ and $\tilde{b} = (0, 1, 0) \parallel y$. Since the orthorhombicity below T_s is small, the angle between a and $\tilde{a}$ deviates only by 0.2° from 45°. It is therefore an excellent approximation to use $a \parallel x' = 1/\sqrt{2}(x + y) \equiv 1/\sqrt{2}(1, 1, 0)$ and $b \parallel y' = 1/\sqrt{2}(y - x) \equiv 1/\sqrt{2}(1, \bar{1}, 0)$.

As the angle of incidence of the exciting photons is as large as 66° in our setup [see Fig. 1(d)], the orientations of $\mathbf{e}_I$ parallel and perpendicular to the xz plane are inequivalent. In particular, $\mathbf{e}_I$ has a projection on the c axis for $\mathbf{e}_I \parallel xz$. This effect was used before [8] and allows one to project out the E_g phonons in the x^*x and x^*y configurations, where $x^* \parallel (x + \alpha z)$ inside the crystal [see Fig. 1(d)]. For $BaFe_2As_2$, the index of refraction is $n' = 2.2 + 2.1i$ at 514 nm, resulting in $\alpha \approx 0.4$ for an angle of incidence of 66°. The corresponding intensity contribution is then 0.16. As a consequence, x^*x and yy are inequivalent whereas $\mathbf{e}_I = x'^* \parallel (x' + \alpha z/\sqrt{2})$ and $\mathbf{e}_I = y'^* \parallel (y' + \alpha z/\sqrt{2})$ are equivalent for having the same projection on the c direction. Upon comparing x^*y and yx, the leakage of the c-axis polarized contributions to the electronic continuum can be tested. In the case here, they are below the experimental sensitivity. The effect of the finite angle of acceptance of the collection optics (±15° corresponding to a solid angle $\tilde{\Omega}$ of 0.21 sr) on the projections of the scattered photons can be neglected.

D. Theoretical calculations

The phonon eigenvectors $Q^{(\nu)}$ (displacement patterns of the vibrating atoms in the branch ν) and the energies of all Raman-active phonons of $BaFe_2As_2$ in the tetragonal ($I4/mmm$) and the orthorhombic ($Fmmm$) phases were obtained from *ab initio* DFT calculations within the Perdew-Burke-Ernzerhof parametrization [31] of the generalized gradient approximation. The phonon frequencies were calculated by diagonalizing the dynamical matrices using the *phonopy* package [32,33]. The dynamical matrices were constructed from the force constants determined from the finite displacements in 2 × 2 × 1 supercells [34]. We used the projector augmented wave approximation [35], as implemented in the Vienna package (VASP) [36–38]. The Brillouin zone for one unit cell was sampled with a 10 × 10 × 10 **k** point mesh, and the plane wave cutoff was set at 520 eV. For the tetragonal phase, we used a Néel-type magnetic order to relax the structure and to obtain the experimental lattice parameters.[1] For the orthorhombic phase, we used the stripelike magnetic order shown in Fig. 1(a).

We have then calculated the complex Raman tensor $\alpha^{(\nu)}_{jk}(\omega_I) = \alpha^{(\nu)\prime}_{jk}(\omega_I) + i\alpha^{(\nu)\prime\prime}_{jk}(\omega_I)$, defined as the derivative of the dielectric tensor elements $\varepsilon_{jk}(\omega_I) = \varepsilon'_{jk}(\omega_I) + i\varepsilon''_{jk}(\omega_I)$ with respect to the normal coordinate of the respective phonon, $Q^{(\nu)}$. Since we are interested only in the resonance behavior of the As phonon, we only needed the derivatives with respect to $Q^{(\mathrm{As})}$,

$$\alpha^{(\mathrm{As})}_{ll}(\omega_I) = \frac{\partial\varepsilon'_{ll}(\omega_I)}{\partial Q^{(\mathrm{As})}} + i\frac{\partial\varepsilon''_{ll}(\omega_I)}{\partial Q^{(\mathrm{As})}}. \quad (1)$$

To calculate the dielectric (tensor) function $\hat{\varepsilon}$ we used the *optics* code package [39] implemented in WIEN2k [40] with the full-potential linearized augmented plane-wave basis. The Perdew-Burke-Ernzerhof generalized gradient approximation [31] was employed as the exchange correlation functional and the basis-size controlling parameter RK_{max} was set to 8.5. A mesh of 400 **k** points in the first Brillouin zone for the self-consistency cycle was used. The DOS and dielectric tensors were computed using a 10 × 10 × 10 **k** mesh. For the dielectric tensor, a Lorentzian broadening of 0.1 eV was introduced.

III. RESULTS AND DISCUSSION

A. Lattice dynamics

The energies and symmetries as obtained from lattice dynamical calculations for tetragonal and orthorhombic

[1]The local correlations in the tetragonal phase are of the stripe type; however, we had to use a pattern that does not break the symmetry, and it is known [18] that the difference in the elastic properties calculated within different magnetic orders is much smaller than between magnetic and nonmagnetic calculations.

TABLE I. Raman-active phonons in $BaFe_2As_2$. The experimental and theoretically determined energies are given in cm^{-1}. In addition, the symmetry correlations between the tetragonal ($I4/mmm$) and orthorhombic ($Fmmm$) structures are shown.

$I4/mmm$				$Fmmm$		
	Exp. (140 K)	Theory			Exp. (60 K)	Theory
A_{1g}	180	168	→	A_g	180	172
B_{1g}	215	218	→	B_{1g}	215	221
$E_g^{(1)}$	130	140	↗	$B_{2g}^{(1)}$	125	110
			↘	$B_{3g}^{(1)}$	135	133
$E_g^{(2)}$	268	290	↗	$B_{2g}^{(2)}$	270	272
			↘	$B_{3g}^{(2)}$	273	287

$BaFe_2As_2$ are compiled in Table I. The four modes in tetragonal $I4/mmm$ symmetry obey $A_{1g} + B_{1g} + 2\ E_g$ selection rules. The eigenvectors are depicted in Fig. 2. In the orthorhombic $Fmmm$ phase, the two E_g modes are expected to split into B_{2g} and B_{3g} modes. Thus, there are six nondegenerate modes in the orthorhombic phase, $A_g + B_{1g} + 2\ B_{2g} + 2\ B_{3g}$. Table I shows the symmetry relations between the tetragonal and orthorhombic phonons.

Since the A_g and B_{1g} eigenvectors remain unchanged upon entering the orthorhombic phase, only those of the B_{2g} and B_{3g} phonons are shown in Fig. 3. For the B_{2g} and B_{3g} phonons, the As and Fe atoms move perpendicular to the c axis and perpendicular to each other. The calculated phonon vibrations agree with previous results for $BaFe_2As_2$ [7], however our energies differ slightly from those reported by Zbiri *et al.* [7]. In particular, we find a splitting between the $B_{2g}^{(1)}$ and $B_{3g}^{(1)}$ phonons.

B. E_g phonons

Table I displays the experimental phonon energies above and below the magneto-structural transition, along with the theoretical values. The $E_g^{(1)}$ phonon found at 130 cm^{-1} above T_s splits into two well-separated lines as predicted (Table I) and shown in Fig. 4. The splitting of the $E_g^{(2)}$ mode at 268 cm^{-1} is small, and the $B_{2g}^{(2)}$ and $B_{3g}^{(2)}$ modes are shifted to higher energies by 2 cm^{-1} and 5 cm^{-1}, respectively.

The theoretical and experimental phonon energies are in agreement to within 14% for both crystal symmetries. The

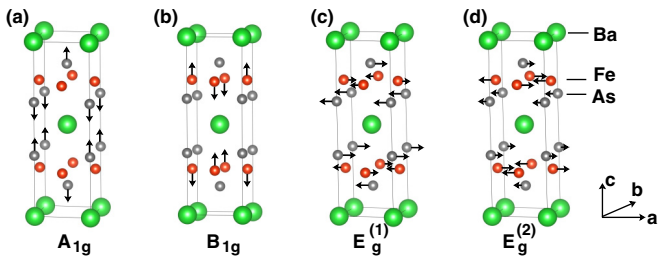

FIG. 2. Raman-active phonons in $BaFe_2As_2$ with the symmetry assignments in the tetragonal crystallographic unit cell abc.

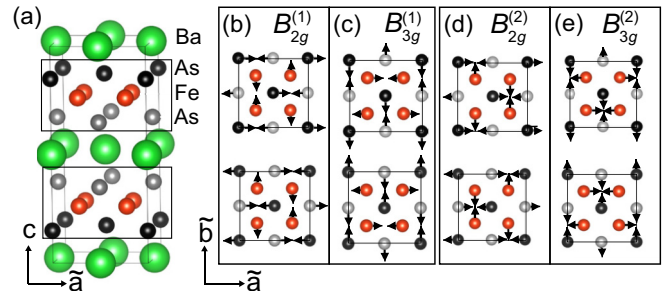

FIG. 3. B_{2g} and B_{3g} phonon modes in $BaFe_2As_2$ with the symmetry assignments in the orthorhombic crystallographic unit cell $\tilde{a}\tilde{b}c$.

splitting between the B_{2g} and B_{3g} modes is overestimated in the calculations.

Previous experiments were performed on twinned crystals [8,41,42] and the B_{2g} and B_{3g} modes were observed next to each other in a single spectrum. An equivalent result can be obtained in detwinned samples by using x'^*y', x'^*x', or RR polarizations where the x and y axes are simultaneously projected (along with the z axis). In neither case can the symmetry of the B_{2g} and B_{3g} phonons be pinned down. Only in a detwinned sample where the xz and yz configurations are projected separately, the B_{2g} and B_{3g} modes can be accessed independently.

Uniaxial pressure along the Fe-Fe direction, as shown by the black arrows in the insets of Fig. 4, determines the orientation of the shorter $\tilde{b}$ axis. This configuration enables us to observe the $B_{2g}^{(1)}$ mode at 125 cm^{-1} and the $B_{3g}^{(1)}$ mode at 135 cm^{-1} in x^*x and, respectively, x^*y polarization configurations, thus augmenting earlier work. With the shorter axis determined by

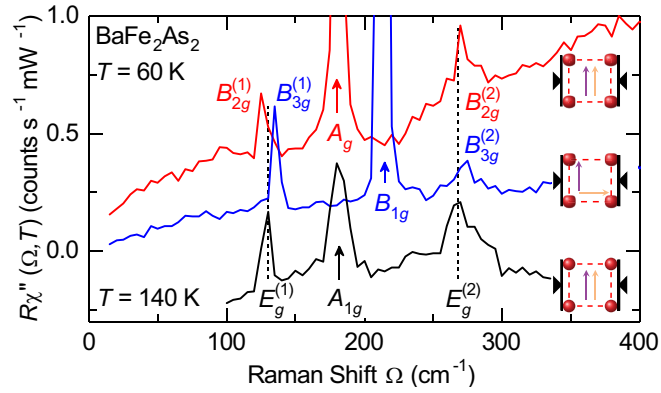

FIG. 4. Phonons in detwinned $BaFe_2As_2$. The spectra at 60 K (red and blue) are displayed with the experimental intensity. The spectrum at 140 K (black) is downshifted by 1.4 counts s^{-1} mW^{-1} for clarity. Each of the two tetragonal E_g phonons (vertical dashed lines) splits into two lines below T_s. The $B_{2g}^{(1)}$ and $B_{3g}^{(1)}$ lines appear at distinct positions for polarizations of the scattered light parallel (blue) and perpendicular (red) to the applied pressure as indicated in the insets. The $B_{2g}^{(2)}$ and $B_{3g}^{(2)}$ phonons are shifted only slightly upward with respect to the $E_g^{(2)}$ mode. Violet and orange arrows indicate the polarizations of the incident and scattered photons, respectively. The black triangles indicate the direction of the applied pressure. The shorter $\tilde{b}$ axis is parallel to the stress.

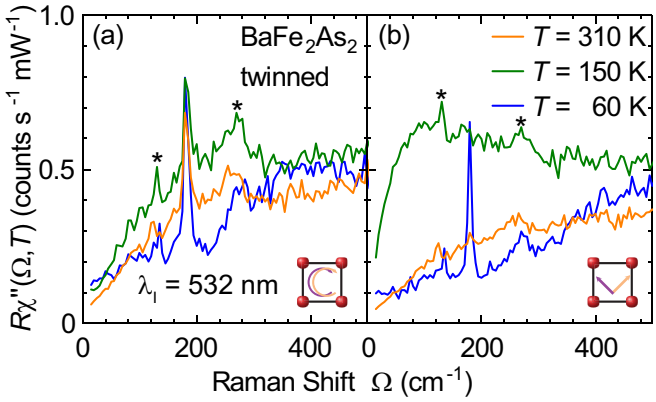

FIG. 5. Raman spectra of twinned $BaFe_2As_2$ at temperatures as indicated. The spectra were measured using $\hbar\omega_I = 2.33$ eV (532 nm). (a) In parallel RR polarization configuration (see inset), the As phonon appears at all temperatures. (b) For crossed light polarizations (ab), the As phonon is present only below the magnetostructural transition at $T_s = 135$ K as reported before [8]. Asterisks mark the E_g modes discussed in Sec. III B.

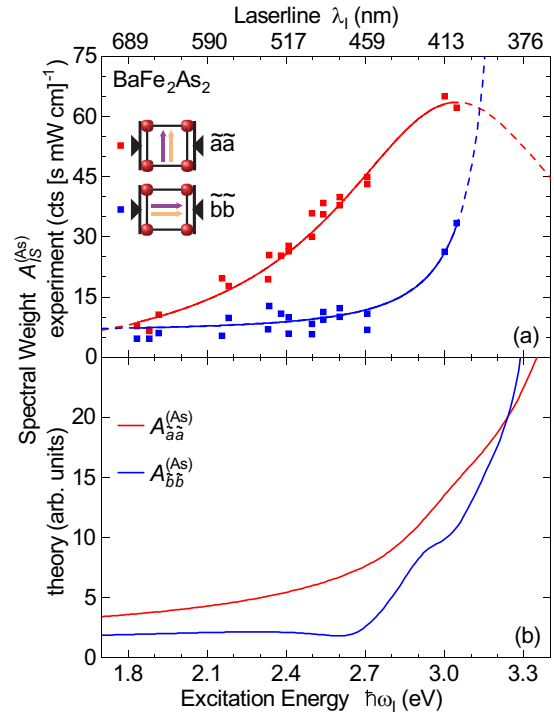

FIG. 6. Spectral weight $A_{IS}^{(As)}(\omega_I)$ of the As phonon as a function of excitation energy and polarization. The top axis shows the corresponding wavelength of the exciting photons. (a) Experimental data. The intensity for parallel light polarizations along the ferromagnetic axis ($\tilde{b}\tilde{b}$, blue squares) is virtually constant for $\hbar\omega_I < 2.7$ eV and increases rapidly for $\hbar\omega_I > 2.7$ eV. For light polarizations along the antiferromagnetic axis ($\tilde{a}\tilde{a}$, red squares), the phonon intensity increases monotonically over the entire range studied. The solid lines are Lorentzian functions whose extrapolations beyond the measured energy interval are shown as dashed lines. (b) Theoretical prediction of $A_{\tilde{a}\tilde{a}}^{(As)}$ (red) and $A_{\tilde{b}\tilde{b}}^{(As)}$ (blue). The curves qualitatively reproduce the experimental data shown in panel (a).

the direction of the stress (insets of Fig. 4) the assignment of the B_{2g} and B_{3g} modes is unambiguous. Since the x^*x spectrum (red) comprises $\tilde{a}\tilde{a}$ and $c\tilde{a}$ polarizations both the A_g and the B_{2g} phonons appear. The x^*y spectrum (blue) includes the B_{1g} ($\tilde{a}\tilde{b}$) and B_{3g} ($c\tilde{b}$) symmetries.

The calculated splitting between the B_{2g} and B_{3g} modes is smaller for the $E_g^{(2)}$ than for the $E_g^{(1)}$ mode, qualitatively agreeing with the experiment. However, in the calculations this difference is entirely due to the different reduced masses for these modes since the $E_g^{(1)}$ and $E_g^{(2)}$ phonon are dominated by As and Fe motions, respectively. In the experiment the splitting for the $E_g^{(2)}$ mode is close to the spectral resolution, indicating an additional reduction of the splitting below that obtained in the calculation. The source of this additional reduction is unclear at the moment.

C. As phonon line intensity

Figure 5 shows low-energy spectra of twinned $BaFe_2As_2$ for (a) RR and (b) ab polarization configurations at 310 (orange), 150 (green), and 60 K (blue). The As phonon at 180 cm^{-1} is the strongest line in the RR spectra at all temperatures as expected and gains intensity upon cooling. In ab polarizations, there is no contribution from the As mode above T_s. Below T_s (blue spectrum), the As phonon assumes a similar intensity as in the RR polarization as reported earlier [8,17]. Due to a finite projection of the incident light polarizations onto the c axis [see Fig. 1(d)] in both RR and ab configurations, the E_g phonons appear in all spectra (asterisks). The electronic continuum has been extensively discussed in previous works [43–47] and is not a subject of the study here.

To understand the appearance of the As line in the crossed ab polarizations, it is sufficient to consider the in-plane components of the A_g Raman tensor,

$$\hat{\alpha}^{(Ag)} = \begin{pmatrix} \alpha_{11} & 0 \\ 0 & \alpha_{22} \end{pmatrix}. \quad (2)$$

The response of this phonon for the polarization configuration ($\mathbf{e}_I$,$\mathbf{e}_S$) is given by $\chi_{IS}^{''(As)} \propto |\mathbf{e}_S^* \cdot \hat{\alpha}^{(Ag)} \cdot \mathbf{e}_I|^2$ (where * means conjugate transposed). In the tetragonal (A_{1g}) case, the two elements are equal, $\alpha_{11} = \alpha_{22}$, and the phonon appears only for $\mathbf{e}_S \parallel \mathbf{e}_I$. In the orthorhombic phase the tensor elements are different, and one can expect the phonon to appear for $\mathbf{e}_S \perp \mathbf{e}_I$ since then the intensity depends on the difference between α_{11} and α_{22}.

In detwinned samples, α_{11} and α_{22} can be accessed independently by using parallel polarizations for the incident and scattered light oriented along either the $\tilde{a}$ or the $\tilde{b}$ axis. In addition, putative imaginary parts of α_{ii} may be detected by analyzing more than two polarization combinations as discussed in Appendix C. Spectra for $\tilde{a}\tilde{a}$ and $\tilde{b}\tilde{b}$ configurations are shown in Fig. 7 of Appendix B and we proceed here directly with the analysis of the phonon spectral weight $A_{IS}^{(As)}(\omega_I)$ as a function of the incident photon excitation energy ($\hbar\omega_I$) and polarization.

Figure 6(a) shows $A_{IS}^{(As)}(\omega_I)$ as derived by fitting the peak with a Voigt function, after subtracting a linear background. Measurements were repeated several times to check the reproducibility. The variation of the spectral weight between

different measurements can be taken as an estimate of the experimental error. For light polarizations parallel to the antiferromagnetic $\tilde{a}$ axis, $A^{(\mathrm{As})}_{\tilde{a}\tilde{a}}(\omega_\mathrm{I})$ (red squares) increases continuously with increasing $\hbar\omega_\mathrm{I}$ whereas $A^{(\mathrm{As})}_{\tilde{b}\tilde{b}}$ (blue squares) stays virtually constant for incident photons in the red and green spectral range, $\hbar\omega_\mathrm{I} < 2.7\,\mathrm{eV}$, and increases rapidly for $\hbar\omega_\mathrm{I} > 2.7\,\mathrm{eV}$. For all wavelengths, the spectral weight is higher for the $\tilde{a}\tilde{a}$ than for the $\tilde{b}\tilde{b}$ configuration.

The variations of $A^{(\mathrm{As})}_{\tilde{a}\tilde{a}}(\omega_\mathrm{I})$ and $A^{(\mathrm{As})}_{\tilde{b}\tilde{b}}(\omega_\mathrm{I})$ display a typical resonance behavior [48], which is expected when the intermediate state of the Raman scattering process is an eigenstate of the electronic system. Then, in second-order perturbation theory, the intensity diverges as $|\hbar\omega_\mathrm{I} - E_0|^{-2}$, where E_0 is the energy difference between an occupied and an unoccupied electronic Bloch state. In real systems having a finite electronic lifetime, a Lorentzian profile is expected. We therefore approximated $A^{(\mathrm{As})}_{1S}(\omega_\mathrm{I})$ with Lorentzians centered at $E_{0,1S}$ as shown by solid lines in Fig. 6(a). From these model functions we determine $E_{0,\tilde{a}\tilde{a}} = 3.1\,\mathrm{eV}$ and $E_{0,\tilde{b}\tilde{b}} = 3.3\,\mathrm{eV}$.

As discussed in the Introduction, the band structure needs to be renormalized so as to account for correlation effects (for details, see Appendix D). To this end, we differentiated three regions: (i) the unoccupied Fe $3d$ bands near the Fermi energy that we rescale uniformly, (ii) the occupied bands below -2.7 eV of predominantly As $4p$ character that remain unchanged, and (iii) the occupied bands between -2.7 eV and the Fermi level derived from hybridized Fe $3d$ and As $4p$ orbitals. Due to this hybridization, the renormalization of the latter bands cannot be performed by simple rescaling. One can anticipate that the optical absorption would set in at energies below 1.8 eV, smaller than our minimal laser energy, if the occupied Fe bands would have been renormalized prior to hybridization with the As bands. Due to the small DOS of the As bands in the range from -2.7 eV to E_F, their contribution to the dielectric function would be small. With this in mind, we simply excluded all occupied bands in this range from the calculations. The effect of these bands, although small, could be accounted for using the DMFT method, which, however, is beyond the scope of our present work.

The results obtained as described above are presented in Fig. 6(b). One can see that the resonances lie in the range $\hbar\omega_\mathrm{I} > 2.7\,\mathrm{eV}$, and our calculations capture both the intensities and the $\tilde{a} - \tilde{b}$ anisotropy in this range rather well. Note that the antiferromagnetic ordering along the $\tilde{a}$ axis entails a backfolding of the electronic bands; we tentatively ascribe the much larger width of the resonance in the $\tilde{a}\tilde{a}$ configuration to this backfolding.

A corollary of our analysis is that resonance effects are the main source of the anomalous intensity of the As phonon in crossed polarizations. The main experimental argument is based on the anisotropic variation of the phonon intensities with $\hbar\omega_\mathrm{I}$ in $\tilde{a}\tilde{a}$ and $\tilde{b}\tilde{b}$ polarization configurations that comes about because of band reconstruction at higher energies. As proposed previously [16], magnetism appears to be the origin of the anisotropy. However, the intensity anisotropy cannot be explained without taking into account the high-energy electronic states.

Finally, we briefly look into the cross-polarization anomaly and find further support for its magnetic origin. In $Ba(Fe_{1-x}Co_x)_2As_2$, the transition temperature T_SDW is several degrees below T_s for a finite x, and one observes that the anomaly of the As phonon does not appear at T_s, but rather at the magnetic transition. For $x = 0.025$, the phonon assumes intensity in crossed polarizations only below T_SDW (see supplementary information of Ref. [46]). For $x = 0.051$, the anomaly appears at T_s, as displayed in Fig. 10 in the Appendix but the spectral weight does not show an order-parameter-like temperature dependence. The increase is nearly linear and saturates below T_SDW at a value which is smaller by approximately a factor of 7 than that in the RR polarization projecting A_g/A_{1g} symmetry. In FeSe, with a structural transition at $T_\mathrm{s} = 89.1\,\mathrm{K}$ but no long-range magnetism [49], the anomalous intensity can also be observed below T_s but the intensity relative to that in the A_g projection is only 1%, as shown in Fig. 11. Similar to $Ba(Fe_{0.949}Co_{0.051})_2As_2$, the spectral weight increases approximately linearly but does not saturate, presumably because FeSe does not develop a long-ranged magnetic order.

IV. CONCLUSION

We studied the Raman scattering for three As phonons, the two E_g, and the one fully symmetric modes, in twin-free $BaFe_2As_2$, accompanied by DFT calculations of Raman intensities, with the goal of clarifying the impact of magnetism on electrons and phonons.

The tetragonal E_g phonons at 130 cm^{-1} ($E_g^{(1)}$) and 268 cm^{-1} ($E_g^{(2)}$) were studied with the laser line at 532 nm and found to split into two modes in the orthorhombic phase. The detwinning allows us to identify the modes at 125 cm^{-1} and 135 cm^{-1} as the $B_{2g}^{(1)}$ and $B_{3g}^{(1)}$ phonons, respectively. DFT calculations predict the symmetries correctly and show that the splitting occurs because of the stripe magnetic order (and not because of the orthorhombic distortion).

The As A_g phonon was studied for various laser lines in the range 1.8 to 3.1 eV. In the ordered phase, the spectral weight of the phonon resonates for an excitation energy of (3.2 ± 0.1) eV. The resonance energy is almost the same for the light polarized along the ferro- or antiferromagnetic directions $\tilde{b}$ and $\tilde{a}$ [for the definition of the axes see Fig. 1(a)], whereas the variation of the spectral weight with the energy of the incident photon is rather different for the $\tilde{b}\tilde{b}$ and $\tilde{a}\tilde{a}$ configurations. The larger width of the resonance in $\tilde{a}\tilde{a}$ configuration can be understood qualitatively in terms of band backfolding along the antiferromagnetic direction.

Our DFT calculations reproduce the anisotropy and the resonance very well for energies above 2.7 eV if we include both the effects of the magnetism and of the correlations-induced renormalization of Fe $3d$ bands. Due to DFT limitations, for energies below 2.7 eV, where correlated Fe $3d$ bands are strongly hybridized with the As bands, our approximation is only semiquantitative. Further studies based, for instance, on DMFT or other many-body methods are needed to test this approximation, apart from experimental verification. As in the case of the E_g phonons, all effects are strongly linked to magnetism. However, in the case of the As phonon, the inclusion of electronic states at high energies is essential because of the observed resonance behavior. Weak-coupling, low-energy physics with magnetism-induced anisotropic electron-phonon

coupling [16] appears insufficient for explaining the anomalous intensity in crossed polarizations.

More generally, our experimental observations and theoretical studies indicate the importance of orbital-dependent band renormalizations and of (nearly) localized ordered spins on the electronic properties at all energy scales.

ACKNOWLEDGMENTS

We gratefully acknowledge discussions with L. Degiorgi and thank him for providing us with raw and analyzed IR data of $BaFe_2As_2$. The work was supported by the Deutsche Forschungsgemeinschaft (DFG) via the Priority Program No. SPP 1458, the Transregional Collaborative Research Centers TRR 80 and TRR 49, and by the Serbian Ministry of Education, Science and Technological Development under Project No. III45018. We acknowledge support by the DAAD through the bilateral project between Serbia and Germany (Grants No. 56267076 and No. 57142964). The collaboration with Stanford University was supported by the Bavaria California Technology Center BaCaTeC (Grant No. A5 [2012-2]). Work in the SIMES at Stanford University and SLAC was supported by the U.S. Department of Energy, Office of Basic Energy Sciences, Division of Materials Sciences and Engineering, under Contract No. DE-AC02-76SF00515. Y.L. and R.V. acknowledge the allotment of computer time at the Centre for Scientific Computing (CSC) in Frankfurt. I.I.M. was supported by ONR through the NRL basic research program and by the Alexander von Humboldt-Stiftung.

APPENDIX A: CALIBRATION OF THE SENSITIVITY

Scattering experiments performed over a wide energy range necessitate an appropriate correction of the data. The quantity of interest is the response function $R\chi''_{IS}(\Omega)$ where $\Omega = \omega_I - \omega_S$ is the Raman shift, and ω_S is the energy of the scattered photons. R includes all experimental constants and units in a way that $R\chi''_{IS}(\Omega)$ is as close as possible to the count rate $\dot{N}^*_{I,S}$, measured for a given laser power $P_I = I_I\hbar\omega_I$ absorbed by the sample. I_I is the number of incoming photons per unit time and I, S refer to both photon energies and polarizations. With A_f, the (nearly) energy-independent area of the laser focus the cross section is given by [50]

$$\frac{\dot{N}^*_{IS}(\Delta\omega_S, \Delta\tilde{\Omega})}{P_I}\hbar\omega_I A_f = R^* r(\omega_S)\frac{d^2\sigma}{d\omega_S d\tilde{\Omega}}\Delta\omega_S\Delta\tilde{\Omega}. \quad \text{(A1)}$$

R^* and $r(\omega_S)$ are a constant and the relative sensitivity, respectively. $r(\omega_S)$ is assumed to be dimensionless and includes energy-dependent factors such as surface losses, penetration depth, and the monochromatic efficiency of the setup. $\Delta\omega_S$ and $\Delta\tilde{\Omega}$ are the bandwidth and the solid angle of acceptance, respectively, and depend both on ω_S. $r(\omega_S)\Delta\omega_S\Delta\tilde{\Omega}$ is determined by calibration and used for correcting the raw data. The resulting rate $\dot{N}_{IS}$ is close to $\dot{N}^*_{IS}$ in the range $\Omega \leqslant 1,000\,\mathrm{cm}^{-1}$ but increasingly different for larger energy transfers mainly for the strong variation of $\Delta\omega_S$. Applying the fluctuation-dissipation theorem, one obtains

$$\frac{\dot{N}_{IS}}{P_I}\hbar\omega_I A_f = R'\frac{d^2\sigma}{d\omega_S d\tilde{\Omega}} = R'\frac{\hbar}{\pi}r_0^2\frac{\omega_S}{\omega_I}\{1 + n(\Omega, T)\}\chi''(\Omega), \quad \text{(A2)}$$

where R' is another constant, which is proportional to $\Delta\omega_S(\omega_0)\Delta\tilde{\Omega}(\omega_0)$, $n(\Omega, T) = [\exp(\frac{\hbar\Omega}{k_B T}) - 1]^{-1}$ is the thermal Bose factor and r_0 is the classical electron radius. Finally, after collecting all energy-independent factors in R we obtain

$$R\chi''_{IS}(\Omega) = \frac{\dot{N}_{IS}}{P_I}\frac{\omega_I^2}{\omega_0\omega_S}\left\{1 - \exp\left(-\frac{\hbar\Omega}{k_B T}\right)\right\}. \quad \text{(A3)}$$

Here, $\omega_0 = 20,000\,\mathrm{cm}^{-1}$ is inserted for convenience to get a correction close to unity. Therefore, the spectra shown reflect the measured number of photon counts per second and mW absorbed power as closely as possible, thus approximately obeying counting statistics as intended. Since the spectra are taken with constant slit width the spectral resolution depends on energy, and narrow structures such as phonons may change their shapes but the spectral weight is energy independent.

APPENDIX B: A_g SPECTRA

Figure 7 shows the complete set of the A_g spectra we measured for detwinned $BaFe_2As_2$ and used for deriving the spectral weights $A^{(As)}_{\tilde{a}\tilde{a}}(\omega_I)$ and $A^{(As)}_{\tilde{b}\tilde{b}}(\omega_I)$ displayed in Fig. 6(a). All spectra were corrected as described in Appendix A. For all spectra, the same constant width of 550 μm of the intermediate slit of the spectrometer was used. This results in an energy-dependent resolution varying between approximately 12 cm^{-1} at 24,630 cm^{-1} (3.05 eV or 406 nm) and 3 cm^{-1} at 14,793 cm^{-1} (1.83 eV or 676 nm). Accordingly, the width of the peak changes as a function of the excitation wavelength and does not reflect the intrinsic line width of the phonon, in particular

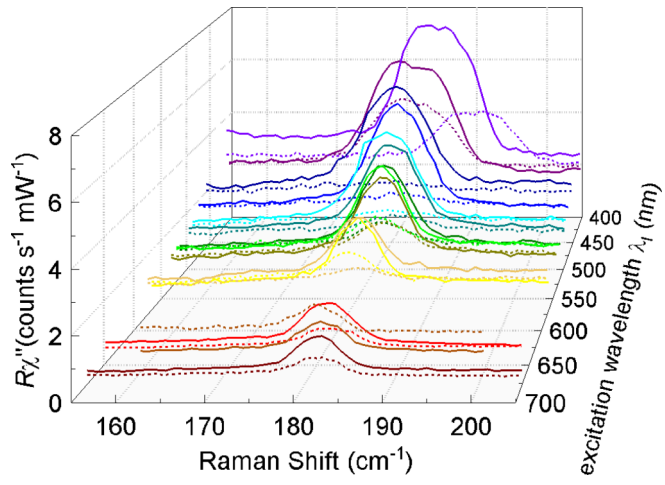

FIG. 7. (Color online.) A_g spectra of detwinned $BaFe_2As_2$ at various laser wavelengths λ_I. We used laser lines between 406 and 676 nm and parallel polarizations of incoming and outgoing photons along the antiferromagnetic ($\tilde{a}\tilde{a}$, solid lines) and the ferromagnetic ($\tilde{b}\tilde{b}$, dashed lines) direction.

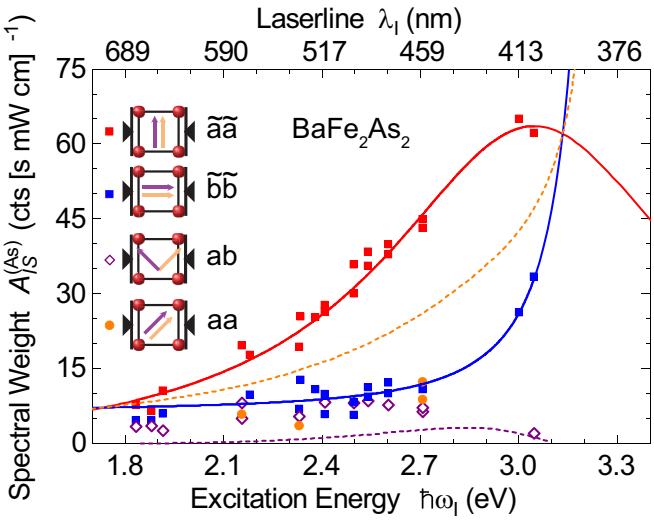

FIG. 8. Spectral weight $A_{IS}^{(\mathrm{As})}(\omega_\mathrm{I})$ of the As phonon as a function of excitation energy and polarization. The top axis shows the corresponding wavelength of the exciting photons. The data for $\tilde{a}\tilde{a}$ (red squares) and $\tilde{b}\tilde{b}$ (blue squares) polarizations as well as the Lorentzian model functions (red and blue solid lines) are identical to Fig. 6(a). The intensity for crossed (ab, purple diamonds) and for aa polarizations (orange dots) is comparable to the intensity found for $\tilde{b}\tilde{b}$ polarization. The purple dashed line is the intensity for ab polarization calculated from the fitted resonance profiles (solid lines) assuming a Raman tensor with real elements. The orange dashed line shows the same calculation for aa polarization.

not for blue photons. The intensity of the peak monotonically increases towards short wavelengths for the $\tilde{a}\tilde{a}$ spectra (solid lines). For light polarized parallel to the ferromagnetic axis ($\tilde{b}\tilde{b}$, dashed lines), the intensity is low for $\lambda_\mathrm{I} > 450$ nm, but strongly increases for $\lambda_\mathrm{I} < 450$ nm. The underlying electronic continuum, which is not a subject of this paper, also changes in intensity as a function of the excitation wavelength. From the spectra, the spectral weight $A_{IS}^{(\mathrm{As})}(\omega_\mathrm{I})$ of the phonon can be derived by fitting a Voigt function to the phonon peak after subtracting a linear background. The width of the Gaussian part of the Voigt function is given by the known resolution of the spectrometer while that of the Lorentzian part reflects the line width of the phonon.

APPENDIX C: SPECTRAL WEIGHT FOR *aa* AND *ab* POLARIZATIONS

Since the ratio $A_{ab}^{(\mathrm{As})}/A_{aa}^{(\mathrm{As})}$ was not in the main focus of our work, Fig. 6(a) displays only part of the data we collected. We also measured spectra in aa and ab configurations (cf. Figs. 1(a) and 8 for the definitions) and find them instructive for two reasons. The aa and ab data (i) can be compared directly with results presented recently [17] and (ii) indicate that the Raman tensor has large imaginary parts which can result only from absorption processes. Figure 8 shows the spectral weights of the As phonon mode for aa and ab polarizations, $A_{aa}^{(\mathrm{As})}(\omega_\mathrm{I})$ (orange circles) and $A_{ab}^{(\mathrm{As})}(\omega_\mathrm{I})$ (open purple diamonds), respectively, for selected wavelengths together with the data and model functions from Fig. 6(a) of the main text. Given the experimental error, the respective intensities for aa and ab polarizations are rather similar and are also comparable to $A_{\tilde{b}\tilde{b}}^{(As)}(\omega_\mathrm{I})$ (blue squares) in the range $1.9 < \hbar\omega_\mathrm{I} \leqslant 2.7$ eV. For $\hbar\omega_\mathrm{I} = 3.05$ eV (406 nm), $A_{ab}^{(As)}(\omega_\mathrm{I})$ is very small, for the yellow-green spectral range $A_{ab}^{(As)}(\omega_\mathrm{I})$ may be even larger than $A_{aa}^{(\mathrm{As})}(\omega_\mathrm{I})$ in qualitative agreement with Ref. [17].

If the elements of the Raman tensor $\hat{\alpha}^{(\mathrm{Ag})}$ [Eq. (2) of the main text] would be strictly real, they could be derived directly from the experimental data as $\alpha_{11} = \sqrt{A_{\tilde{a}\tilde{a}}^{(As)}}$ and $\alpha_{22} = \sqrt{A_{\tilde{b}\tilde{b}}^{(As)}}$. Then, the phonon's spectral weight expected for all other polarizations could be calculated right away, and $A_{aa}^{(As)}$ is just the average of $A_{\tilde{a}\tilde{a}}^{(As)}$ and $A_{\tilde{b}\tilde{b}}^{(As)}$ (dashed orange line in Fig. 8). Obviously, there is no agreement with the experimental values for $A_{aa}^{(As)}$ (orange circles).

$A_{ab}^{(As)}$ can be determined in a similar fashion. In Fig. 8, we show the expected spectral weight as purple dashed line. The dependence on ω_I is again derived from the model functions describing the resonance (full red and blue lines). Also for $A_{ab}^{(As)}$, the mismatch between experiment (open purple diamonds) and expectation (purple dashed line) is statistically significant, and one has to conclude that the assumption of real tensor elements in the orthorhombic phase is not valid.

This effect is not particularly surprising in an absorbing material and was in fact discussed earlier for the cuprates [51,52]. For the Fe-based systems, the possibility of complex Raman tensor elements for the As phonon was not considered yet. Our experimental observations show that the complex nature of $\hat{\alpha}^{(\mathrm{Ag})}$ is crucially important and that the imaginary parts of α_{11} and α_{22} must have opposite sign to explain the observed enhancement of $A_{ab}^{(\mathrm{As})}(\omega_\mathrm{I})$ and the suppression of $A_{aa}^{(\mathrm{As})}(\omega_\mathrm{I})$ with respect to the values expected for real tensor elements (dashed orange and purple lines in Fig. 8).

In summary, the results for $A_{aa}^{(As)}(\omega_\mathrm{I})$ and $A_{ab}^{(As)}(\omega_\mathrm{I})$ along with those for $A_{\tilde{a}\tilde{a}}^{(As)}(\omega_\mathrm{I})$ and $A_{\tilde{b}\tilde{b}}^{(As)}(\omega_\mathrm{I})$ support our point of view that absorption processes are important for the proper interpretation of the Raman data. Currently, we cannot imagine anything else but resonance effects due to interband transitions as the source.

APPENDIX D: BAND STRUCTURE

The DFT band structure is shown in Fig. 9. Bands above E_F stem predominantly from Fe $3d$ orbitals (brown) while for $E < -2.7$ eV As $4p$ orbitals prevail (black). For a suitable comparison to the experiment these Fe bands are renormalized by a factor between 2 and 3 [53–56] while no renormalization is needed for the As bands. The bands between -2.7 eV and E_F are of mixed Fe/As character and are left out when calculating the dielectric tensor as is illustrated by the grey shade in Fig. 9. Only transitions between the ranges [-5.5 eV,-2.7 eV] and [0,2.6 eV], highlighted by turqouise rectangles, are taken into account. Thus for photon energies below 2.7 eV, the absorption in our calculations originates predominantly from the Drude response whereas for $\hbar\omega_\mathrm{I} > 2.7$ eV the results become increasingly realistic since they include interband absorption. In either case, we use a phenomenological damping of 0.1 eV. We determine the dielectric tensor and the Raman tensor as described in Sec. II D on the basis of this renormalized

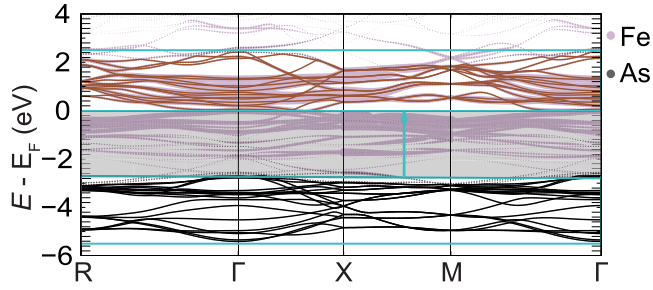

FIG. 9. DFT band structure. Bands predominantly from Fe states are shown in brown, bands predominantly from As states in black. The shaded region from −2.7 eV to E_F contains bands of mixed character and is blacked out for the calculation of the dielectric tensor. Only transitions between the bands within the turquoise frames are included.

band structure. While the $\tilde{a} - \tilde{b}$ anisotropy is qualitatively reproduced for all energies ω_I as shown in Fig. 6(b) of the main text, the two other experimental quantities, $A_{ab}^{(As)}(\omega_I)$ (purple) and $A_{aa}^{(As)}(\omega_I)$ (orange) shown in Fig. 8 here, are not captured properly simply because the imaginary parts of the theoretically determined tensor elements $\alpha_{ii}^{(As)''}$ become very small below 2.7 eV. To describe $A_{aa}^{(As)}(\omega_I)$ and $A_{ab}^{(As)}(\omega_I)$, absorption processes which lead to imaginary parts of the Raman tensor are necessary. Upon phenomenologically introducing imaginary parts of $\hat{\alpha}$ for low energies, which cut off at 2.7 eV where the correct absorption takes over, full agreement can be achieved. However, a solution on a microscopic basis becomes possible only by using schemes that include many-body effects beyond DFT.

APPENDIX E: INTERRELATION OF THE A_g PHONON ANOMALY AND MAGNETISM IN $Ba(Fe_{1-x}Co_x)_2As_2$ AND FeSe

Similarly as in $BaFe_2As_2$, the anomalous intensity of the A_g phonon in crossed polarizations is also linked to magnetic order in other Fe-based systems as shown for $Ba(Fe_{1-x}Co_x)_2As_2$ at $x = 0.025$ a while ago [46] and more recently for $EuFe_2As_2$, NaFeAs, LaFeAsO, and FeSe [17]. Here, we add a few more results which support our interpretation. Figure 10(a) shows Raman spectra in ab polarization of $Ba(Fe_{1-x}Co_x)_2As_2$ with $x = 5.1\%$ having $T_s = 60.9$ K and $T_{SDW} = 50.0$ K. The As mode appears below T_s and gains strength upon cooling. Figure 10(b) shows the corresponding spectral weight as a function of temperature. In the nematic phase $T_{SDW} < T < T_s$, the phonon spectral weight increases almost linearly upon cooling (rather than order-parameter-like), becomes constant in the magnetic phase for $T < T_{SDW}$ and reaches approximately 15% of that in the fully symmetric channel (A_g/A_{1g}).

In FeSe, the Se phonon appears also in the ab spectra as shown in Fig. 11(a) when the temperature is lowered below the structural phase transition at $T_s \approx 90$ K. Upon cooling [Fig. 11(b)], the spectral weight of the phonon increases almost linearly for crossed polarizations (ab, black squares), but stays virtually constant across the phase transition for parallel light polarizations [RR, orange circles in Fig. 11(b)]. As opposed to $Ba(Fe_{1-x}Co_x)_2As_2$, no saturation of the spectral weight

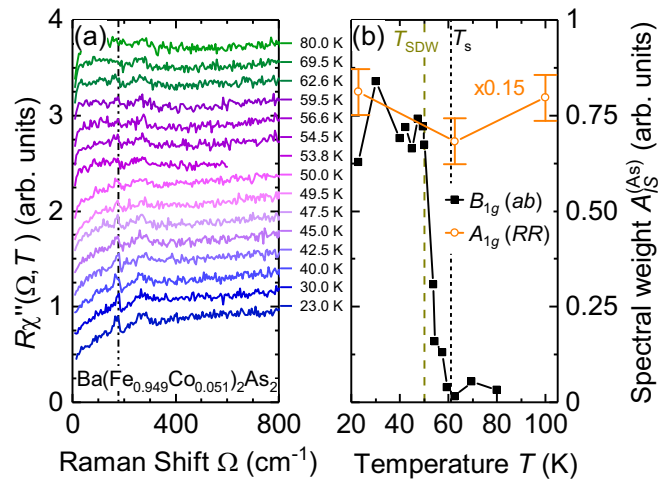

FIG. 10. As phonon in crossed polarizations for $Ba(Fe_{1-x}Co_x)_2As_2$ at $x = 0.051$. (a) Raw data for temperatures as indicated. The phonon position is shown as a vertical dash-dotted line. The spectra are shifted vertically for clarity. (b) Temperature dependence of the spectral weight. The spectral weight in A_{1g} symmetry (orange circles) was multiplied by 0.15. T_s and T_{SDW} are indicated as vertical dashed lines.

in ab polarizations is found, likely because FeSe shows no long-range magnetic order down to the lowest temperatures [49]. Only about 1% of the spectral weight of the A_{1g} spectra (RR) is found in crossed polarizations here, in contrast to $BaFe_2As_2$ and $Ba(Fe_{1-x}Co_x)_2As_2$, where the spectral weight of the phonon is larger (Figs. 5 and 10).

The nearly linear temperature dependence in both FeSe and $Ba(Fe_{1-x}Co_x)_2As_2$ and the larger saturation value in magnetically ordered $Ba(Fe_{1-x}Co_x)_2As_2$ indicate that the anomalous intensity is more likely related to magnetism than to the orthorhombic distortion.

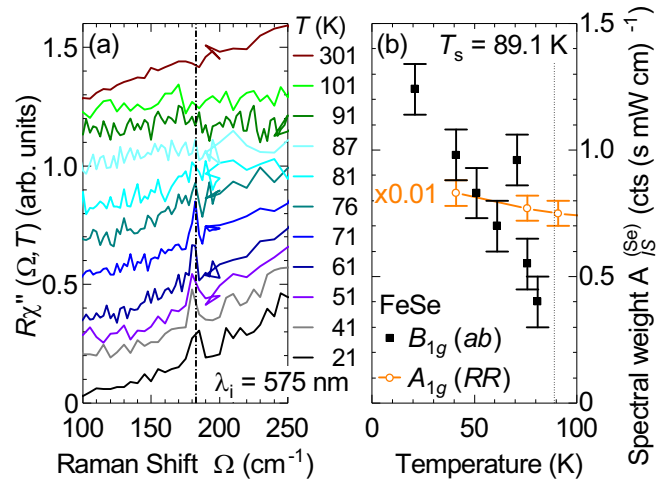

FIG. 11. Se phonon in crossed polarization for FeSe. (a) Raw data for temperatures as indicated. The phonon position is shown as dash-dotted line. The spectra are shifted vertically for clarity. (b) Temperature dependence of the spectral weight. The spectral weight in A_{1g} symmetry (orange circles) was multiplied by 0.01. T_s is indicated as vertical dotted line.

[1] A. S. Sefat and D. J. Singh, Chemistry and electronic structure of iron-based superconductors, MRS Bull. **36**, 614 (2011).

[2] F. Wang, S. A. Kivelson, and D.-H. Lee, Nematicity and quantum paramagnetism in FeSe, Nat. Phys. **11**, 959 (2015).

[3] Y. Gallais and I. Paul, Charge nematicity and electronic Raman scattering in iron-based superconductors, C. R. Phys. **17**, 113 (2016).

[4] M. Yi, Y. Zhang, Z.-X. Shen, and D. Lu, Role of the orbital degree of freedom in iron-based superconductors, npj Quantum Mater. **2**, 57 (2017).

[5] A. E. Böhmer and A. Kreisel, Nematicity, magnetism and superconductivity in FeSe, J. Phys.: Condens. Matter **30**, 023001 (2018).

[6] T. Yildirim, Strong Coupling of the Fe-Spin State and the As-As Hybridization in Iron-Pnictide Superconductors from First-Principle Calculations, Phys. Rev. Lett. **102**, 037003 (2009).

[7] M. Zbiri, H. Schober, M. R. Johnson, S. Rols, R. Mittal, Y. Su, M. Rotter, and D. Johrendt, Ab initio lattice dynamics simulations and inelastic neutron scattering spectra for studying phonons in $BaFe_2As_2$: Effect of structural phase transition, structural relaxation, and magnetic ordering, Phys. Rev. B **79**, 064511 (2009).

[8] L. Chauvière, Y. Gallais, M. Cazayous, A. Sacuto, M. A. Méasson, D. Colson, and A. Forget, Doping dependence of the lattice dynamics in $Ba(Fe_{1-x}Co_x)_2As_2$ studied by Raman spectroscopy, Phys. Rev. B **80**, 094504 (2009).

[9] L. Chauvière, Y. Gallais, M. Cazayous, M. A. Méasson, A. Sacuto, D. Colson, and A. Forget, Raman scattering study of spin-density-wave order and electron-phonon coupling in $Ba(Fe_{1-x}Co_x)_2As_2$, Phys. Rev. B **84**, 104508 (2011).

[10] M. Rahlenbeck, G. L. Sun, D. L. Sun, C. T. Lin, B. Keimer, and C. Ulrich, Phonon anomalies in pure and underdoped $R_{1-x}K_xFe_2As_2$ (R = Ba, Sr) investigated by Raman light scattering, Phys. Rev. B **80**, 064509 (2009).

[11] P. Kumar, A. Kumar, S. Saha, D. V. S. Muthu, J. Prakash, S. Patnaik, U. V. Waghmare, A. K. Ganguli, and A. K. Sood, Anomalous Raman scattering from phonons and electrons of superconducting $FeSe_{0.82}$, Solid State Commun. **150**, 557 (2010).

[12] R. Mittal, L. Pintschovius, D. Lamago, R. Heid, K.-P. Bohnen, D. Reznik, S. L. Chaplot, Y. Su, N. Kumar, S. K. Dhar, A. Thamizhavel, and T. Brueckel, Measurement of Anomalous Phonon Dispersion of $CaFe_2As_2$ Single Crystals Using Inelastic Neutron Scattering, Phys. Rev. Lett. **102**, 217001 (2009).

[13] V. Gnezdilov, Y. G. Pashkevich, P. Lemmens, D. Wulferding, T. Shevtsova, A. Gusev, D. Chareev, and A. Vasiliev, Interplay between lattice and spin states degree of freedom in the FeSe superconductor: Dynamic spin state instabilities, Phys. Rev. B **87**, 144508 (2013).

[14] V. Gnezdilov, Y. Pashkevich, P. Lemmens, A. Gusev, K. Lamonova, T. Shevtsova, I. Vitebskiy, O. Afanasiev, S. Gnatchenko, V. Tsurkan, J. Deisenhofer, and A. Loidl, Anomalous optical phonons in FeTe chalcogenides: Spin state, magnetic order, and lattice anharmonicity, Phys. Rev. B **83**, 245127 (2011).

[15] A. Akrap, J. J. Tu, L. J. Li, G. H. Cao, Z. A. Xu, and C. C. Homes, Infrared phonon anomaly in $BaFe_2As_2$, Phys. Rev. B **80**, 180502 (2009).

[16] N. A. García-Martínez, B. Valenzuela, S. Ciuchi, E. Cappelluti, M. J. Calderón, and E. Bascones, Coupling of the As A_{1g} phonon to magnetism in iron pnictides, Phys. Rev. B **88**, 165106 (2013).

[17] S.-F. Wu, W.-L. Zhang, V. K. Thorsmølle, G. F. Chen, G. T. Tan, P. C. Dai, Y. G. Shi, C. Q. Jin, T. Shibauchi, S. Kasahara, Y. Matsuda, A. S. Sefat, H. Ding, P. Richard, and G. Blumberg, Magneto-elastic coupling in Fe-based superconductors (2017), arXiv:1712.01896 [cond-mat.supr-con].

[18] I. I. Mazin, M. D. Johannes, L. Boeri, K. Koepernik, and D. J. Singh, Problems with reconciling density functional theory calculations with experiment in ferropnictides, Phys. Rev. B **78**, 085104 (2008).

[19] J.-H. Chu, J. G. Analytis, C. Kucharczyk, and I. R. Fisher, Determination of the phase diagram of the electron-doped superconductor $Ba(Fe_{1-x}Co_x)_2As_2$, Phys. Rev. B **79**, 014506 (2009).

[20] S. A. J. Kimber, A. Kreyssig, Y.-Z. Zhang, H. O. Jeschke, R. Valentí, F. Yokaichiya, E. Colombier, J. Yan, T. C. Hansen, T. Chatterji, R. J. McQueeney, P. C. Canfield, A. I. Goldman, and D. N. Argyriou, Similarities between structural distortions under pressure and chemical doping in superconducting $BaFe_2As_2$, Nat. Mater. **8**, 471 (2009).

[21] M. G. Kim, R. M. Fernandes, A. Kreyssig, J. W. Kim, A. Thaler, S. L. Bud'ko, P. C. Canfield, R. J. McQueeney, J. Schmalian, and A. I. Goldman, Character of the structural and magnetic phase transitions in the parent and electron-doped $BaFe_2As_2$ compounds, Phys. Rev. B **83**, 134522 (2011).

[22] M. Rotter, M. Tegel, and D. Johrendt, Superconductivity at 38 K in the Iron Arsenide $(Ba_{1-x}K_x)Fe_2As_2$, Phys. Rev. Lett. **101**, 107006 (2008).

[23] J.-H. Chu, J. G. Analytis, K. D. Greve, P. L. McMahon, Z. Islam, Y. Yamamoto, and I. R. Fisher, In-plane resistivity anisotropy in an underdoped iron arsenide superconductor, Science **329**, 824 (2010).

[24] J. J. Ying, X. F. Wang, T. Wu, Z. J. Xiang, R. H. Liu, Y. J. Yan, A. F. Wang, M. Zhang, G. J. Ye, P. Cheng, J. P. Hu, and X. H. Chen, Measurements of the Anisotropic in-Plane Resistivity of Underdoped FeAs-Based Pnictide Superconductors, Phys. Rev. Lett. **107**, 067001 (2011).

[25] A. Dusza, A. Lucarelli, F. Pfuner, J.-H. Chu, I. R. Fisher, and L. Degiorgi, Anisotropic charge dynamics in detwinned $Ba(Fe_{1-x}Co_x)_2As_2$, Europhys. Lett. **93**, 37002 (2011).

[26] A. Dusza, A. Lucarelli, A. Sanna, S. Massidda, J.-H. Chu, I. R. Fisher, and L. Degiorgi, Anisotropic in-plane optical conductivity in detwinned $Ba(Fe_{1-x}Co_x)_2As_2$, New J. Phys. **14**, 023020 (2012).

[27] M. Nakajima, T. Liang, S. Ishida, Y. Tomioka, K. Kihou, C. H. Lee, A. Iyo, H. Eisaki, T. Kakeshita, T. Ito, and S. Uchida, Unprecedented anisotropic metallic state in undoped iron arsenide $BaFe_2As_2$ revealed by optical spectroscopy, Proc. Natl. Acad. Sci. USA **108**, 12238 (2011).

[28] M. Yi, D. Lu, J.-H. Chu, J. G. Analytis, A. P. Sorini, A. F. Kemper, B. Moritz, S.-K. Mo, R. G. Moore, M. Hashimoto, W.-S. Lee, Z. Hussain, T. P. Devereaux, I. R. Fisher, and Z.-X. Shen, Symmetry-breaking orbital anisotropy observed for detwinned $Ba(Fe_{1-x}Co_x)_2As_2$ above the spin density wave transition, Proc. Natl. Acad. Sci. USA **108**, 6878 (2011).

[29] T. Liang, M. Nakajima, K. Kihou, Y. Tomioka, T. Ito, C. H. Lee, H. Kito, A. Iyo, H. Eisaki, T. Kakeshita, and S. Uchida, Effects of uniaxial pressure and annealing on the resistivity of $Ba(Fe_{1-x}Co_x)_2As_2$, J. Phys. Chem. Solids **72**, 418 (2011).

[30] E. C. Blomberg, A. Kreyssig, M. A. Tanatar, R. M. Fernandes, M. G. Kim, A. Thaler, J. Schmalian, S. L. Bud'ko, P. C. Canfield,

A. I. Goldman, and R. Prozorov, Effect of tensile stress on the in-plane resistivity anisotropy in $BaFe_2As_2$, Phys. Rev. B **85**, 144509 (2012).

[31] J. P. Perdew, K. Burke, and M. Ernzerhof, Generalized Gradient Approximation Made Simple, Phys. Rev. Lett. **77**, 3865 (1996).

[32] A. Togo, F. Oba, and I. Tanaka, First-principles calculations of the ferroelastic transition between rutile-type and $CaCl_2$-type SiO_2 at high pressures, Phys. Rev. B **78**, 134106 (2008).

[33] A. Togo and I. Tanaka, First principles phonon calculations in materials science, Scr. Mater. **108**, 1 (2015).

[34] K. Parlinski, Z. Q. Li, and Y. Kawazoe, First-Principles Determination of the Soft Mode in Cubic ZrO_2, Phys. Rev. Lett. **78**, 4063 (1997).

[35] P. E. Blöchl, Projector augmented-wave method, Phys. Rev. B **50**, 17953 (1994).

[36] G. Kresse and J. Hafner, Ab initio molecular dynamics for liquid metals, Phys. Rev. B **47**, 558 (1993).

[37] G. Kresse and J. Furthmüller, Efficient iterative schemes for ab initio total-energy calculations using a plane-wave basis set, Phys. Rev. B **54**, 11169 (1996).

[38] G. Kresse and J. Furthmüller, Efficiency of ab-initio total energy calculations for metals and semiconductors using a plane-wave basis set, Comput. Mater. Sci. **6**, 15 (1996).

[39] C. Ambrosch-Draxl and J. O. Sofo, Linear optical properties of solids within the full-potential linearized augmented planewave method, Comput. Phys. Commun. **175**, 1 (2006).

[40] P. Blaha, K. Schwarz, G. K. H. Madsen, D. Kvasnicka, and J. Luitz, WIEN2k: *An Augmented Plane Wave Plus Local Orbitals Program for Calculating Crystal Properties* (Technische Universität Wien, Wien, 2001).

[41] X. Ren, L. Duan, Y. Hu, J. Li, R. Zhang, H. Luo, P. Dai, and Y. Li, Nematic Crossover in $BaFe_2As_2$ under Uniaxial Stress, Phys. Rev. Lett. **115**, 197002 (2015).

[42] W.-L. Zhang, A. S. Sefat, H. Ding, P. Richard, and G. Blumberg, Stress-induced nematicity in $EuFe_2As_2$ studied by Raman spectroscopy, Phys. Rev. B **94**, 014513 (2016).

[43] K.-Y. Choi, D. Wulferding, P. Lemmens, N. Ni, S. L. Bud'ko, and P. C. Canfield, Lattice and electronic anomalies of $CaFe_2As_2$ studied by Raman spectroscopy, Phys. Rev. B **78**, 212503 (2008).

[44] L. Chauvière, Y. Gallais, M. Cazayous, M. A. Méasson, A. Sacuto, D. Colson, and A. Forget, Impact of the spin-density-wave order on the superconducting gap of $Ba(Fe_{1-x}Co_x)_2As_2$, Phys. Rev. B **82**, 180521 (2010).

[45] S. Sugai, Y. Mizuno, R. Watanabe, T. Kawaguchi, K. Takenaka, H. Ikuta, Y. Takayanagi, N. Hayamizu, and Y. Sone, Spin-density-wave gap with Dirac nodes and two-magnon Raman scattering in $BaFe_2As_2$, J. Phys. Soc. Jpn. **81**, 024718 (2012).

[46] F. Kretzschmar, T. Böhm, U. Karahasanović, B. Muschler, A. Baum, D. Jost, J. Schmalian, S. Caprara, M. Grilli, C. Di Castro, J. H. Analytis, J.-H. Chu, I. R. Fisher, and R. Hackl, Critical spin fluctuations and the origin of nematic order in $Ba(Fe_{1-x}Co_x)_2As_2$, Nat. Phys. **12**, 560 (2016).

[47] V. K. Thorsmølle, M. Khodas, Z. P. Yin, C. Zhang, S. V. Carr, P. Dai, and G. Blumberg, Critical quadrupole fluctuations and collective modes in iron pnictide superconductors, Phys. Rev. B **93**, 054515 (2016).

[48] M. Cardona, *Resonance Phenomena*, 1st ed. (Springer-Verlag, Berlin, Heidelberg, 1982) Chap. 2, pp. 19–178.

[49] S.-H. Baek, D. V. Efremov, J. M. Ok, J. S. Kim, J. van den Brink, and B. Büchner, Orbital-driven nematicity in FeSe, Nat. Mater. **14**, 210 (2014).

[50] B. Muschler, W. Prestel, L. Tassini, R. Hackl, M. Lambacher, A. Erb, S. Komiya, Y. Ando, D. C. Peets, W. N. Hardy, R. Liang, and D. A. Bonn, Electron interactions and charge ordering in CuO_2 compounds, Eur. Phys. J. Special Topics **188**, 131 (2010).

[51] T. Strach, J. Brunen, B. Lederle, J. Zegenhagen, and M. Cardona, Determination of the phase difference between the Raman tensor elements of the A_{1g}-like phonons in $SmBa_2Cu_3O_{7-\delta}$, Phys. Rev. B **57**, 1292 (1998).

[52] C. Ambrosch-Draxl, H. Auer, R. Kouba, E. Y. Sherman, P. Knoll, and M. Mayer, Raman scattering in $yba_2cu_3o_7$: A comprehensive theoretical study in comparison with experiments, Phys. Rev. B **65**, 064501 (2002).

[53] S. L. Skornyakov, A. V. Efremov, N. A. Skorikov, M. A. Korotin, Y. A. Izyumov, V. I. Anisimov, A. V. Kozhevnikov, and D. Vollhardt, Classification of the electronic correlation strength in the iron pnictides: The case of the parent compound $BaFe_2As_2$, Phys. Rev. B **80**, 092501 (2009).

[54] Y. X. Yao, J. Schmalian, C. Z. Wang, K. M. Ho, and G. Kotliar, Comparative study of the electronic and magnetic properties of $BaFe_2As_2$ and $BaMn_2As_2$ using the Gutzwiller approximation, Phys. Rev. B **84**, 245112 (2011).

[55] J. Ferber, K. Foyevtsova, R. Valentí, and H. O. Jeschke, LDA + DMFT study of the effects of correlation in LiFeAs, Phys. Rev. B **85**, 094505 (2012).

[56] S. Backes, H. O. Jeschke, and R. Valentí, Microscopic nature of correlations in multiorbital AFe_2As_2(A = K, Rb, Cs): Hund's coupling versus Coulomb repulsion, Phys. Rev. B **92**, 195128 (2015).